



LAWRENCE
LIVERMORE
NATIONAL
LABORATORY

In-situ transmission electron microscopy of crystal growth-mode transitions during rapid solidification of a hypoeutectic Al-Cu alloy

J. T. McKeown, A. K. Kulovits, C. Liu, K. Zweiacker, B. W. Reed, T. LaGrange, J. M. K. Wiezorek, G. H. Campbell

September 24, 2013

Acta Materialia

Disclaimer

This document was prepared as an account of work sponsored by an agency of the United States government. Neither the United States government nor Lawrence Livermore National Security, LLC, nor any of their employees makes any warranty, expressed or implied, or assumes any legal liability or responsibility for the accuracy, completeness, or usefulness of any information, apparatus, product, or process disclosed, or represents that its use would not infringe privately owned rights. Reference herein to any specific commercial product, process, or service by trade name, trademark, manufacturer, or otherwise does not necessarily constitute or imply its endorsement, recommendation, or favoring by the United States government or Lawrence Livermore National Security, LLC. The views and opinions of authors expressed herein do not necessarily state or reflect those of the United States government or Lawrence Livermore National Security, LLC, and shall not be used for advertising or product endorsement purposes.

***In-situ* transmission electron microscopy of crystal growth-mode transitions during rapid solidification of a hypoeutectic Al-Cu alloy**

Joseph T. McKeown¹, Andreas K. Kulovits², Can Liu², Kai Zwiack², Bryan W. Reed¹, Thomas LaGrange¹, Jörg M. K. Wiezorek² and Geoffrey H. Campbell¹

¹ Condensed Matter and Materials Division, Lawrence Livermore National Laboratory,
Livermore, CA 94550, USA

² Department of Mechanical Engineering and Materials Science, University of Pittsburgh,
Pittsburgh, PA 15261, USA

Abstract

The rapid solidification dynamics of a pulsed-laser-melted hypoeutectic Al-Cu thin-film alloy were monitored using *in-situ* transmission electron microscopy with high spatial and temporal resolutions. Direct observation of the solid-liquid interface during the transformation allowed measurements of the time-evolving solidification front morphology and velocity. Transitions in the growth mode were detected and related to acceleration and instability at the solidification front. A banded structure that forms during instability at high solidification front velocities, previously only observed *ex situ* in postmortem analyses, was imaged during formation, providing insight to the growth mechanisms of this banded morphology.

1. Introduction

Solidification processing is an important step in the fabrication of metals and alloys, which are used in engineering components and systems for application in electronic, electro-magnetic, and electro-optical micro-devices, as well as biomedical, petrochemical, energy, and transportation technologies [1]. Manipulation of the solidification conditions and constitutional effects at the solidification interface induces microstructural changes in the resultant solid and can therefore be used to control properties. Far-from-equilibrium solidification processing of metals and alloys (e.g., using electron or laser beams) can involve very large thermal gradients of $\sim 10^5\text{--}10^7\text{ K}\cdot\text{m}^{-1}$ and rapid cooling rates of $10^5\text{--}10^7\text{ K}\cdot\text{s}^{-1}$ [2]. Such extreme solidification conditions enable severe microstructural refinement of grains and precipitates, extension of solid solubility limits, non-equilibrium phase formation including amorphous phases, and partitionless solidification. The latter produces solid alloy crystals with the same composition as the liquid, establishing a state of maximum extension of the solid solubility. Hence, rapid solidification of alloys has been widely studied and recognized as a viable processing route to obtain unique microstructures with potentially advantageous properties that are not obtainable with conventional solidification processes [3].

Prior studies of rapid solidification have shown particular interest in Al-Cu alloys with Al-rich compositions due to the large body of well-defined thermophysical, optical, and solidification data that exists for this system [4-7]. The Al-rich portion of the Al-Cu equilibrium phase diagram [8], shown in Fig. 1, contains a eutectic with terminal phases of $\alpha\text{-Al}$ and $\theta\text{-Al}_2\text{Cu}$. The eutectic temperature and composition are 548°C and $\sim 17\text{at}\%$, respectively. Numerous studies on the rapid solidification of Al-Cu alloys [9-20] have reported observations of various microstructural features, including degenerate eutectics [10,17,19], cellular and dendritic

morphologies [11-13,17,19], and banded structures [10,12,14,15,17,19]. Solidification microstructure selection maps have been determined as a function of composition and solidification velocity [17,19] for Al-rich Al-Cu alloys that were rapidly solidified after surface melting with a scanned continuous-wave laser. Furthermore, a solidification-front-velocity dependent extension of the range for eutectic growth has been established using Al-rich Al-Cu alloys as a model system and was rationalized in terms of a competitive growth model [21]. Rapid solidification under far-from-equilibrium conditions can also occur in nanoscale systems with planar thin-film geometries [1,2]. Extreme solidification front velocities in the range of 1–100 m·s⁻¹ have been reported for solidification in metal thin films after pulsed-laser melting [22-24]. In order to develop better understanding of the processes responsible for establishing the unique and often scale-refined microstructures obtained by rapid alloy solidification, direct experimental observations of the dynamics associated with the solidification front would be desirable and instructive. However, the high velocity of the transformation front during rapid solidification processes renders microscopic experimental *in-situ* imaging and characterization of the evolving microstructure and solidification front morphology extremely challenging. For instance, consider a solidification front moving with a relatively slow velocity of 1 mm·s⁻¹. *In-situ* imaging experiments conducted with conventional data acquisition rates of 30 frames per second corresponds to a temporal resolution of ~33 ms per frame and, limited by motion blur, would offer spatial resolution of only ~33 μm. Hence, prior reports on the microstructure evolution during rapid solidification have been based almost entirely on post-mortem analyses [13,15,17].

In-situ experiments with the required nanoscale spatiotemporal resolution to monitor rapid solidification processes are enabled by the dynamic transmission electron microscope

(DTEM) [25-32] at Lawrence Livermore National Laboratory and have been performed previously on pure Al metal thin films [24]. Direct imaging and diffraction-based TEM studies can provide unique insight into the mechanisms and kinetics governing rapid solidification processes. For example, *in-situ* DTEM studies of rapid solidification in pure Al determined a deceleration of the morphologically planar solidification front [24]. Changes in solidification front velocity are expected when growth-mode transitions occur, as reported for Al-Cu alloys [16,17,19]. Past reports on solidification front velocities during rapid solidification usually represent averages for the complete liquid-solid transformation and fail to detect changes in velocity [33].

Here, Al-Cu alloys constrained to a thin-film geometry serve as a model system toward the development of state-of-the-art *in-situ* TEM techniques for experimental research on nanoscale phenomena during rapid solidification. Hypoeutectic alloys with composition Al-7at%Cu were pulsed-laser melted and the microstructural evolution during subsequent rapid solidification was monitored *in situ* in the TEM at high spatial and temporal resolutions to provide unique observations and measurements regarding the dynamics under these far-from-equilibrium conditions. Post-solidification microstructural analyses were performed to complement the *in-situ* DTEM studies.

2. Experimental Procedures

Hypoeutectic Al-7at%Cu (Al-15wt%Cu) alloy thin films were deposited to a thickness of ~80 nm by electron-beam evaporation (Pascal Technologies Dual E-Beam Deposition System) onto 50-nm-thick amorphous Si₃N₄ support films of 500×500 μm windowed TEM grids (Ted Pella, Inc.). The alloy films were deposited in high vacuum (base pressure below 5×10⁻⁸ Torr) at a rate of 2–2.5 nm·s⁻¹ with the substrates held at 298 K.

In-situ rapid solidification experiments were conducted in the DTEM [25-32] using a 1064-nm wavelength, ~15-ns pulsed Nd:YAG laser with a Gaussian beam profile ($1/e^2$ diameter of $135 \pm 5 \text{ } \mu\text{m}$) to provide the thermal stimulus that drives melting. A laser pulse fluence of $\sim 300 \pm 10 \text{ mJ}\cdot\text{cm}^{-2}$ incident at 45° was used to melt the Al-Cu thin films. Imaging of the rapid solidification dynamics in the DTEM was performed with a 15-ns duration electron pulse containing a sufficient number of electrons ($> 2 \times 10^9$) for single-shot bright-field (BF) diffraction-contrast imaging. The imaging electron pulse is generated at a preset delay time relative to the pump pulse using a Nd:YLF laser pulse, resulting in pulsed photoemission of electrons from the modified electron source. The 15-ns duration of the electron pulse represents the temporal resolution of the DTEM imaging experiments of the transient, solidifying structure in the alloys.

The alloy thin films have been characterized by TEM analyses before and after rapid solidification in the DTEM. Pre-solidification analyses were performed using a JEOL JEM-2100F TEM/STEM operated at 200 kV and equipped with an X-ray energy dispersive spectrometer (EDS) (Oxford Instruments) and a Philips CM300 FEG ST TEM operated at 300 kV and equipped with a Gatan Imaging Filter (GIF) and EDS (Oxford Instruments). Post-solidification analysis was conducted in the Philips CM300. This TEM is also equipped with an orientation mapping system (ASTAR/DigiSTAR, NanoMEGAS) that was used for analyzing grain orientations of rapidly solidified regions of the thin film. Large-area orientation maps were obtained by indexing electron diffraction patterns acquired with an electron probe size of 10 nm from locations separated by 100-nm steps across a $\sim 20 \text{ } \mu\text{m} \times 20 \text{ } \mu\text{m}$ scan area. Bright-field and high-angle annular dark-field (HAADF) STEM imaging was conducted with a JEOL JEM-2010F TEM/STEM instrument operated at 200 kV.

3. Results

3.1. Initial state

Fig. 2(a) shows a BF TEM image of the Al-Cu alloy thin film prior to solidification experiments, revealing that the initial state of the film was nanocrystalline with an average grain size of ~50 nm. Fig. 2(b) shows an experimental selected-area electron diffraction pattern from the initial film with a simulated diffraction pattern. Fig. 2(c) presents the rotationally integrated profile of the experimental diffraction pattern in Fig. 2(b). The diffraction data reveals that the film consisted of nanocrystalline grains of the equilibrium α -Al and θ -Al₂Cu phases. This phase separation was associated with natural aging of the alloy thin films after deposition and should have little effect on the solidification experiments, as the laser-irradiated regions of the film were completely melted during the experiments, which will yield a liquid with the nominal hypoeutectic composition of the film, Al-7at%Cu.

3.2. Time-resolved observations of rapid solidification

Pulsed-laser melting and re-solidification of the alloy films was conducted by a series of pump-probe experiments at different time delays in the DTEM. Fig. 3 presents selections of BF TEM micrographs from two separate time-delay series. For each micrograph, the time delay after the pump pulse initiated melting of the alloy is shown as an inset. Scale markers are different for the two separate series of experiments and are shown for the first images in each series of Fig. 3(a) and (b), respectively. The two time-resolved series were recorded at different magnifications to reveal various features of the microstructure evolution during rapid solidification. Each BF TEM micrograph in Fig. 3 is obtained from a separate solidification experiment performed on an as-deposited region of the film at a different time delay, such that the full set of images yields an ensemble-average picture of the solid-liquid interface propagation. Prior to melting, the film

showed little contrast at this magnification due to the fine-scale grain size, as shown in the first frame of Fig. 3(a). The solid-liquid interface is indicated in the 15 μs and 10 μs images of Fig. 3(a) and 3(b), respectively. The liquid melt pool appears featureless and lacks contrast, while the newly formed solid phase consuming the alloy melt displays contrast features in the BF TEM micrographs as a result of grain growth and crystallographic orientation.

Salient features of the solidification process are evident upon inspection of the time-resolved images of Fig. 3. The solid-liquid interface was curved on the micron length scale (the melt pool was elliptical due to the angle between the laser and specimen, with dimensions of $\sim 27\ \mu\text{m}$ and $35\ \mu\text{m}$ for the minor and major axes, respectively), but appears morphologically smooth at length scales on the order of the film thickness, with no evidence of constitutional dendritic growth due to morphological instability at the solidification front. These instabilities can result from solute rejection into the liquid, creating a constitutionally undercooled boundary layer ahead of the advancing solid-liquid interface. At a delay time between 20–25 μs , there was a marked change in the curvature of the solid-liquid interface to a more faceted, chevron-like appearance, which is apparent in both 25 μs images. This change in the morphology of the interface was accompanied by a sudden increase in the velocity of the solidification front, seen by the noticeable decrease in the size of the melt pool. The morphology and velocity changes coincide with the onset of a large, central microstructural zone. The complex structure of this central zone is a banded structure (most clearly seen in the 25 μs image of Fig. 3(a), as indicated), common to many rapidly solidified alloys [15,34-37] when the solidification conditions approach a critical velocity leading to an instability [38,39] at the solid-liquid interface. Finally, the alloy was completely re-solidified by $\sim 30\ \mu\text{s}$ after the laser-induced melting of the alloy film.

Even at the relatively low magnifications of the BF TEM micrographs in Fig. 3, it is apparent that morphologically distinct microstructural zones formed during the rapid solidification process. Around the periphery of the initial melt pool, a region of small grains with random orientations developed. The random crystallographic orientations of these grains are evident based on the contrast, where darker grains signify a stronger diffraction condition, e.g., closer to a zone-axis orientation. This perimeter region of small, morphologically equiaxed grains generated a characteristic columnar zone, with columnar grains growing into the melt pool opposite to the direction of heat flow. In this thin-film geometry, heat is primarily transported in the plane of the film, with a negligible temperature gradient in the film-normal direction within ~50 ns after the laser pulse. Radiative cooling is negligible for the times and temperature scales of these experiments, given the low emissivity of the 93% pure aluminum. Thus the great majority of the heat flow is radially outward, from the hot liquid to the cooler surrounding areas. The solid film surrounding the liquid alloy melt pool is analogous to a mold surface in a casting or the solid bulk substrate in a surface melting scenario, with the primary difference being the nanoscale thickness of the film, making the experimental geometry essentially two-dimensional. The columnar zone abruptly terminated at a large, central microstructural zone consisting of what appears to be a few large grains with a complex intragranular structure that contains the banded structure mentioned previously. The nature of and relationships among all of the microstructural zones will be further discussed in subsequent sections.

3.3. Post-solidification characterization of microstructure and morphology

Fig. 4 displays a montage of BF TEM images showing the resultant microstructure of the rapid solidification process across an entire pulsed-laser-melted region. Three microstructural zones are evident, as labeled in Fig. 4: (1) a heat-affected zone containing a small-grained

thermal exposure experienced in this perimeter region during the pulsed-laser heating and the subsequent transport of heat.

The microstructure shown in Fig. 5 is part of a larger heat-affected zone that results from the relatively soft profile of the Gaussian laser spot, so that significant photon energy is absorbed beyond the melt-pool range. The heat-affected zone was observed in low-magnification post-mortem SEM images and extends radially $\sim 30\text{--}35\text{ }\mu\text{m}$ beyond the melt pool. A heat-affected zone has previously been identified in pure Al thin films after pulsed-laser melting under comparable experimental conditions [41]. This heat-affected zone can be related to the equilibrium phase diagram (see Fig. 1) as the region of the exposed film that experienced temperatures below the melting temperature ($\sim 615^\circ\text{C}$ for an Al-7at%Cu alloy) but high enough to undergo further microstructural evolution. The temperature profile through the heat-affected zone will decay with distance from the edge of the melt pool from the melting temperature, through the mixed-phase ($\alpha+L$) region of the equilibrium phase diagram to the eutectic temperature ($\sim 615^\circ\text{C}$ to 548°C), and then to temperatures below the eutectic temperature. At temperatures below the eutectic, coarsening and further phase separation will drive the morphology evolution of the initial ($\alpha+\theta$) microstructure. At temperatures above the eutectic but below the melting temperature, nucleation of the primary solidification product phase, the pro-eutectic α -Al micro-constituent, can potentially occur in conjunction with this coarsening and phase separation.

The region of the film shown in Fig. 5 was adjacent to the initial melt pool and therefore likely heated to a temperature above the eutectic in the ($\alpha+L$) mixed-phase region of the phase diagram. This microstructure consists of a typical hypoeutectic structure, with grains of pro-eutectic α -Al phase surrounded by a Cu-enriched phase. Based on equilibrium considerations

using the phase diagram, this surrounding Cu-enriched phase was initially a liquid after laser melting. If the cooling rate was slow enough to maintain near-equilibrium solidification, sufficient solute partitioning would increase the composition of this liquid to the eutectic composition and a eutectic structure or micro-constituent would form. However, a eutectic micro-constituent with a typical lamellar morphology was not detected. This potentially signals a deviation from equilibrium solidification even during this early stage of the alloy solidification process.

The zone 2 microstructure is illustrated in the BF TEM and ADF STEM images shown in Fig. 6(a) and 6(b), respectively. Zone 2 is a transition zone to growth-controlled solidification, where grains of α -Al solid solution crystallize and grow inward toward the center of the melt pool. This growth commenced, based on the time-resolved images, $\sim 10 \mu\text{s}$ after melting with the pulsed laser. As indicated in the micrographs of Fig. 6, α -Al solid solution grains grow with shapes elongated along the direction of growth opposite the direction of heat flow, clearly deviating significantly from the equiaxed grain shapes in zone 1 and in the alloy prior to pulsed-laser melting. During zone 2 growth, solute rejection into the liquid will cause perturbations along the solid-liquid interface [42]. As these perturbations amplify, the growth rates at the peaks and troughs of these perturbations begin to differ. Unlike at troughs, solute can be rejected laterally at the peaks, resulting in an increased undercooling and growth rate [42]. This excess solute will accumulate in the perturbation troughs, leading to the formation of a cellular/dendritic structure, as is seen directly beneath the upper dashed line in Fig. 6(b). This cellular/dendritic morphology rapidly transitions to a columnar structure with a eutectic growth mode, indicated by the lower dashed line in Fig. 6(b). This columnar morphology can reach an optimum growth form by an occlusion process, where competitive growth of these grains in zone 2 resulted in a

subset of these grains expanding laterally sufficiently rapidly to obstruct growth of some neighboring grains. The grains surviving the occlusion process continued to grow inward toward the center of the melt pool, producing the morphologically columnar microstructure of zone 3. During the transition from zone 2 to zone 3, the crystal growth mode changed from a hypoeutectic mode with pro-eutectic α -Al solid solution grain formation to eutectic solidification. This can be inferred from the appearance of the Cu-enriched intragranular precipitates (bright contrast in the DF STEM image of Fig. 6(b)) throughout the morphologically elongated grains comprised of an α -Al solid-solution matrix (dark contrast in Fig. 6(b)). These zone 3 grains with a columnar morphology represent eutectic solidification and the transition to this eutectic solidification mode occurred approximately along the lower dashed line in Fig. 6(b).

The morphologically columnar grains of eutectic solidification product form the majority of the zone 3 microstructure. These large, elongated grains stretch from the edge of the melt pool (zone 2) to the central banded structure of zone 3, and they range in length from ~ 10 – $15\ \mu\text{m}$ and width from ~ 0.5 – $2\ \mu\text{m}$ with a thickness of $0.08\ \mu\text{m}$. Typically, between six to eight of the morphologically columnar eutectic grains of zone 3 are involved in another growth mode transition, which is associated with formation of the central banded solidification microstructure. Fig. 7(a) shows BF TEM montage images of multiple grains that constitute the columnar morphology of zone 3. Each of these columnar grains was tilted to a strongly diffracting zone-axis orientation and therefore appears dark in contrast. Three types of columnar grains are shown in Fig. 7(a): 1) grains that terminate at or before the central banded structure; 2) and 3) grains that form the central banded structure. The majority of columnar grains in zone 3 are of type 1. The occlusion process continues in zone 3, which is particularly evident in the image showing the type-1 columnar grains, where three grains are in a zone-axis orientation—two of these

grains are occluded by neighboring grains while one columnar grain terminates at the central banded structure. The type-2 grains are those that develop into large banded grains in the central region. The type-3 grains are those that wrap around the type-2 grains and together with the latter constitute the central banded morphological region. In all solidification experiments involving Al-7at%Cu alloys, only two type-2 grains developed, both along the major axis of the elliptical melt pool at the two points of highest curvature on the solid-liquid interface (see Fig. 3 and Fig. 4). These type-2 grains are large in area, spanning ~ 15 grain diameters along the solid-liquid interface. A number of type-3 grains form, growing along isotherms in the melt pool and wrapping around the type-2 grains. As will be shown, this growth morphology is directly related to the solidification front velocity and instability at the solid-liquid interface, where the instability initiates the transition to the third growth mode.

An automated crystallographic orientation mapping system was used to acquire and index diffraction patterns from the zone 3 region of the pulsed-laser-melted microstructure shown in Fig. 4. As in postmortem analysis of rapidly solidified Al thin films [24], the ASTAR/Digistar orientation mapping system from NanoMEGAS [43-45] was used to acquire and index position-sensitive electron diffraction patterns. This orientation mapping provided more robust and easier identification of grains, grain boundaries, and grain boundary character than conventional diffraction-contrast imaging in the TEM. A virtual BF image, formed using the central spot intensities from each diffraction pattern acquired across the scanned region, with the corresponding orientation map are provided in Fig. 7(b). The orientations plotted, indicated in the color-coded stereographic triangle legend, are parallel to the solidification front growth direction (labeled GD for selected grains in the figure). As shown in the orientation map (Fig. 7(b)), no distinct, preferential crystallographic growth direction is evident in the zone 3 grains,

implying randomness in growth direction selection. This is consistent with planar/columnar or non-dendritic growth, where columnar grains grow with their growth axes parallel to the direction of heat flow, regardless of crystal orientation [42] (as opposed to dendritic growth where, for fcc crystals, preferred growth occurs along the $\langle 001 \rangle$ direction that is closest to parallel with the direction of heat flow). Clearly, six different columnar grains are responsible for the formation of the central banded morphology during rapid solidification of the hypoeutectic Al-Cu alloy, and these six grains are labeled A–F in Fig. 7(b). The grains A and B are two large, single type-2 grains with identical orientations as their respective parent columnar grains, while grains C–F are type-3 “wraparound” grains. It should be noted that the growth directions of these six grains, based on the orientation map in Fig. 7(b), are all close to or along a $\langle 001 \rangle$ -type direction. While further investigation of the texture and growth directions of these grains is necessary, it may be that during the growth-mode transition to cellular/dendritic growth in zone 2, a $[001]$ growth direction was established along the direction of maximum heat flow.

The type-2 grains of zone 3 exhibit a morphologically banded internal microstructure, as shown in the BF and HAADF STEM images of Fig. 7(c). This banded structure consists of alternating light and dark bands, as observed in prior studies [15,17,37], where the light bands are microsegregation-free α -Al, a product of partitionless crystal growth, and the dark bands are composed of the same eutectic micro-constituent that is present throughout the columnar structure. The arrows in Fig. 7(c) delineate the type-3 “wraparound” grain labeled D in Fig. 7(b), which also exhibits the banded morphology. This banding exists in both the type-2 and type-3 grains and occurs in both types of grains perpendicular to the direction of heat flow (and temperature gradient). The first band that appears in all of the rapidly solidified films is always the light contrast, microsegregation-free band. The overall arrangement of the alternating bands

of partitionless and eutectic solidification product in the central structure appears to follow the profile of isotherms within the elliptical melt pool. The time-resolved bright-field TEM images from the DTEM time-delay series shown in Fig. 3 provide direct evidence for the increase in crystal growth rate associated with the change in growth mode in zone 3 that produces the central banded morphology. Composition analyses by EDS have shown that the featureless regions exhibit the nominal alloy composition, consistent with partitionless solidification, while selected-area diffraction patterns obtained from the eutectic solidification product in both the columnar and banded regions of zone 3 indicate that the precipitates with Cu-enriched compositions are consistent with θ -phase-related structures [4,11]. A continuous Cu-enriched phase at the boundaries between all columnar grains was also observed in zone 3, evident in Fig. 6(b). This phase results from Cu rejection at the solid-liquid interface during solidification. The curvature of the solid-liquid interface at boundaries between solidifying grains will be higher than the curvature along the rest of the interface, due to the crystallographic misorientation between neighboring solidifying columnar grains, leading to enhanced rejection of Cu at the boundaries and the observed formation of a Cu-enriched phase at all boundaries.

3.4. Kinetics

The solidification front velocities along the semi-major, a , and semi-minor, b , axes of the elliptical melt pool, v_s^a and v_s^b , have been determined* and are shown in Fig. 8. The varying

* The solidification front velocities were determined by first measuring the position of the solid-liquid interface with time, x_t^a and x_t^b , relative to the initial position, x_0^a and x_0^b , from the time-resolved TEM images, yielding the following exponential functions of time for the position of the solid-liquid interface along the two axes: $x_t^a = 0.0189\exp[0.2855t]$ ($R^2 = 0.977$) and $x_t^b = 0.0155\exp[0.2848t]$ ($R^2 = 0.973$). Evaluating the derivatives of these functions at each time, t ,

curvature along the solid-liquid interface results in a range of solidification front velocities, with the maximum and minimum velocities occurring, respectively, along the semi-major and semi-minor axes of the melt pool, as these points of the solidification front exhibit the highest and lowest curvatures, respectively. The velocity for the time interval up to 20 μs corresponds entirely to the columnar eutectic product formation in zone 3 and was associated with increasing velocities up to $\sim 1.5 \text{ m}\cdot\text{s}^{-1}$. The transition in growth mode to the central banded morphology was observed in the DTEM experiments at $\sim 20\text{--}25 \text{ }\mu\text{s}$ delay time after pulsed-laser melting of the alloy. The average velocities associated with the formation of the central banded morphology were in the range of $\sim 4.5 \text{ m}\cdot\text{s}^{-1}$. On average, the solidification front accelerated during the rapid solidification of the hypoeutectic Al-7at%Cu alloy, reaching a maximum velocity of almost $7 \text{ m}\cdot\text{s}^{-1}$ at the points of highest curvature (along the semi-major axis of the melt pool) of the transformation interface. These points of maximum velocity were the points of origin for the two large grains associated with formation of the vast majority of the central banded morphology (the instability at the solid-liquid interface initiated at these two points).

4. Discussion

The nanoscale spatiotemporal resolution offered by the DTEM enabled direct, *in-situ* experimental observations of the solid-liquid interface evolution, transformation products, and growth-mode changes occurring at the transformation front during rapid solidification in hypoeutectic Al-Cu alloy thin films after pulsed-laser-induced melting. These time-resolved observations yielded measurements of the solidification front velocity and how it varied with time. Combining the *in-situ* DTEM observations with the postmortem *ex-situ* TEM observations provides an in-depth description of the solidification microstructure as a function of kinetics.

gave the instantaneous velocities of the solidification front, v_s^a and v_s^b , along the semi-major and semi-minor axes of the melt pool.

Overall, evolution of the velocity of the solidification interface is expected. The solid-liquid interface has zero velocity until growth begins in zone 2 and then accelerates, presumably reaching a steady state or accelerating at a lesser rate than in zone 2 during the zone 3 columnar eutectic growth, to the point of instability at the transformation interface. While the experimental DTEM images show the microstructure evolution associated with the measured acceleration of the solidification front at unprecedented spatial and temporal resolutions, they do not always capture with complete accuracy the velocity evolution during the growth-mode changes. In zone 2, the observed microstructure and solidification front velocities are consistent with a velocity that is a smooth function of time, which can be estimated with reasonable precision. In zone 3, observations of the resultant microstructure and measurement of the overall time scale, coupled with the general phenomenology of rapid solidification [15,17,19,37], strongly suggests an extremely unsteady, oscillatory velocity with time. This oscillatory velocity evolution can be represented schematically, though the quantitative details cannot be captured with microsecond-scale ensemble-average measurements.

The overall time-varying velocity of the solidification front is illustrated schematically in Fig. 9. This plot of the velocity evolution (solid curve) was constructed by combining qualitative interpretation of the *in-situ* and postmortem *ex-situ* results of this study and prior postmortem *ex-situ* studies [15,17,19,37] with phenomenological modeling [37] of rapid solidification morphologies. Experimentally observed morphologies were related to velocity evolution using the considerations of solidification theory [37,42] when developing Fig. 9, which predicts, for growth in a positive temperature gradient, the solidification front to evolve morphologically from planar to cellular to dendritic to cellular to banded to planar with increasing velocity. The phenomenological model [37] considered undercoolings at a solid-liquid interface for dendritic

and eutectic alloys and found a range of velocities that led to oscillatory instability at the solidification front. Two critical velocities that depend on solute trapping and attachment kinetics were predicted and correspond to transitions from dendritic/eutectic growth to bands and from bands to completely partitionless solidification. Thus, the previously published model [37] provided estimates of velocities with the appropriate order of magnitude to understand this oscillatory instability associated with the banded morphology.

Fig. 9 also overlaps the experimentally determined time-varying velocity of the solidification front (dashed curve, as in Fig. 8) with the qualitative schematic plot. This illustrates the difficulties associated with capturing the evolution of the solidification front using microsecond ensemble-average measurements, particularly during rapid acceleration and instability propagation. The capability to image a *single* solidification event at multiple time delays with variable, fine temporal spacing has recently been enabled by upgrades to the DTEM instrument [46,47] and will be the focus of future rapid solidification work. However, we can still correlate the observed solidification microstructure with the measured time-varying velocity at the temporal spacings employed in the current DTEM experiments, using postmortem images of the microstructure and Fig. 9 as a guide to understanding the microstructure evolution and changes in growth mode.

Motion of the solidification front does not commence until $\sim 10 \mu\text{s}$ after pulsed-laser melting. The $10\text{-}\mu\text{s}$ delay between melting and initial motion of the solid-liquid interface can be explained by considering the difference in laser absorptivity between the solid and liquid states of the alloy. When irradiated with a pulsed laser, the absorptivity of aluminum undergoes a stepwise increase at the melting temperature [48]. This absorption of liquid aluminum is $\sim 1.5\text{--}2$ times greater [48,49] than that of aluminum in the solid state. Melting of the thin film occurs at

picosecond timescales [50] and will commence at the upper surface due to skin-depth effects. The liquid melt pool therefore absorbs significantly more energy during pulsed-laser irradiation (15 ns), leading to a steeper initial thermal gradient in the liquid relative to the solid thin film. A mixed-phase solid-liquid region will also be present around the perimeter of the melt pool after pulsed-laser melting but it is expected to collapse in much less than 1 μ s based on the thermal conductivities, heat of fusion, and estimated temperature gradients present at the end of the laser pulse. The first 10 μ s after laser irradiation should therefore be characterized by rapid collapse of this mixed-phase region followed by evolution of the temperature gradients in the solid and liquid phases toward values that provide the thermal conditions for growth. At these temperatures (i.e., roughly 600°C based on the phase diagram (Fig. 1)), the thermal conductivities, κ , of the solid and liquid Al-Cu alloy are, respectively, ~ 185 and $85 \text{ W}\cdot\text{m}^{-1}\cdot\text{K}^{-1}$ [7,51], while the thermal conductivity of the amorphous silicon nitride membrane is $\sim 10 \text{ W}\cdot\text{m}^{-1}\cdot\text{K}^{-1}$ [52]. Thus, heat will flow predominantly through the solid alloy film during cooling.

Growth began in zone 2 at $\sim 10 \mu$ s after pulsed-laser melting of the alloy film. This initial growth of the solidification front was evidenced by the elongation of α -Al grains along the growth direction (Fig. 6). Due to the small grain size, a varying crystallographic orientation was present along this initial solid-liquid interface, and therefore the growth front advanced with a columnar morphology.

As solidification progresses a constitutionally undercooled liquid will develop as a result of Cu rejection from the solidified alloy, leading to Cu enrichment in a boundary layer ahead of the solid-liquid interface. As discussed previously, this solute rejection will allow local perturbations along the solid-liquid interface to extend into the undercooled liquid, and growth proceeds as these perturbations advance the solidification front. The first growth-mode change

occurred in zone 2, as a morphological instability due to this constitutional undercooling at the solidification front leads to formation of a cellular/dendritic structure, indicated by the upper dashed line in Fig. 6(b). Cellular growth occurs at the limit of constitutional undercooling [42], which depends on the thermal gradients at the solid-liquid interface, and the transition from cells to dendrites occurs at a transition velocity, v_t , given by the critical velocity at the limit of constitutional undercooling divided by the equilibrium partition coefficient, v_c/k_e [53]. For an Al-7at.%Cu alloy ($k_e=0.17$) this transition velocity corresponds to an approximately six-fold increase in the velocity. Based on the postmortem images of the microstructure in Fig. 6, the solidification front became morphologically unstable, indicated by the cellular/dendritic appearance between the dashed lines in the figure, and likely transitioned rapidly from planar to cellular to dendritic. A second growth-mode change occurred soon after this transition to cellular/dendritic growth, indicated by the lower dashed line in Fig. 6(b). The constitutional undercooling facilitated evolution from a hypoeutectic to a eutectic growth mode, consistent with the implications of Burden and Hunt [21,54,55], which indicate that given sufficient driving forces a rapidly moving solidification front in hypoeutectic Al-Cu alloys prefers kinetically modified eutectic growth over dendritic growth of the primary pro-eutectic micro-constituent, resulting in an entirely eutectic structure. Given the spatial dimensions of the zone 2 microstructure, ~750–1000 nm along the growth direction, and the measured position of the solid-liquid interface as a function of time, it is likely that these two changes in growth mode occurred, and zone 2 solidification was complete, during the first ~50–100 ns after solidification began. This implies a rapid acceleration during zone 2 solidification, which corresponds to a rapidly increasing driving force for solidification. This rapid acceleration in zone 2 is illustrated schematically in the inset of Fig. 9.

The second growth-mode change to eutectic growth marks the transition from zone 2 to zone 3. In zone 3, the columnar morphology with an entirely eutectic structure grew while the solidification front continued to accelerate and the velocity rapidly approached and exceeded $1 \text{ m}\cdot\text{s}^{-1}$, as measured from the time-resolved experiments (see Fig. 8). The acceleration was presumably not as rapid as in zone 2, as schematically illustrated in Fig. 9, since there were no changes in growth mode until instability development leading to the banded morphology.

At this transition to eutectic growth, the solidification front velocity likely exceeded the rate of solute transport at the interface. A large undercooling develops rapidly to temperatures below the eutectic temperature (548°C) due to heat extraction and constitutional effects, leading to rapid acceleration. In this high-velocity regime, the velocity is no longer a strong function of the temperature gradient and further undercooling and acceleration are driven by capillarity effects and attachment kinetics [56]. The observed eutectic structure in zone 3 is consistent with predictions of eutectic solidification modes in hypoeutectic alloys for sufficiently high solidification front velocities [21,42,54-56]. The analyses of Burden and Hunt [21,54,55] show that the cellular/dendrite tip temperature decreases as velocity increases, the spatial temperature gradient does not significantly affect the reduction in tip temperature, and at high-velocity conditions the undercooling at the interface becomes proportional to the square root of the velocity ($\Delta T_0 \propto \sqrt{v}$). This implies increased undercooling at the accelerating solid-liquid interface and therefore it is reasonable to reach a condition where the velocity-modified growth mode produces a kinetically preferred or velocity-modified eutectic. A range of alloy compositions that undergo eutectic solidification for a specific solidification front velocity, or coupled zone, exists, and eutectic solidification can occur at compositions other than the thermodynamic eutectic composition [42,56]. This coupled zone typically expands and shifts its

composition range as the velocity and undercooling are increased, and the coupled zone, which consists of an entirely eutectic microstructure rather than simultaneous growth of primary dendrites and interdendritic eutectic, represents an undercooled compositional region where the eutectic grows more rapidly than dendrites of either of the two terminal phases. Therefore, at the large velocities of the crystallization front observed in the alloy DTEM experiments, it can be expected that the eutectic growth mode becomes dominant over the cellular or dendritic growth modes for the hypoeutectic composition Al-Cu alloys.

The morphology of this eutectic structure (see Fig. 6 and Fig. 7(c)) is clearly not a typical lamellar eutectic structure. The morphology of the eutectic structure resembles the chaotic, degenerate eutectic structure observed in previous rapid solidification studies of hypoeutectic alloys [10,11,16]. This velocity-modified eutectic structure may be a transient growth structure that is kinetically favored during rapid solidification, which could develop into the steady-state lamellar eutectic, as has been observed [57]. While, as stated previously, electron diffraction patterns obtained from the eutectic solidification product indicate a mixture of α and θ -phase-related structures, attempts to measure the compositions of the two phases using energy-dispersive spectrometry (EDS) in the TEM have been complicated by the size and embedded morphology of the Cu-enriched phase. These measurements have indicated that both phases have compositions close to the nominal composition of the as-deposited alloy (7at%Cu). Further investigations are required before a definitive assessment of this eutectic product can be provided, but it is certainly plausible that, given the rapid solidification process, a mixture of α and θ -related phases could form where each phase has the same composition as the liquid [58].

Zone 3 solidification of the columnar eutectic product progressed with increasing velocity to the point of absolute stability [38,39], at which point there is a third change in growth

mode that produces the central banded morphology. This banded structure, detected postmortem in prior studies [15,17,37], has not been previously observed *in situ*, and insight to the mechanism of formation due to this instability can be inferred from the time-resolved images. This third solidification growth-mode change occurred at $\sim 20\text{--}25\ \mu\text{s}$ after pulsed-laser melting ($\sim 10\text{--}15\ \mu\text{s}$ after solidification began) and a velocity of $\sim 1.5\ \text{m}\cdot\text{s}^{-1}$. This velocity is consistent with previous reports on the formation of the banded morphology in rapidly solidifying hypoeutectic Al-Cu alloys [15,17,19,37]. The instabilities at the transformation interface occur when the eutectic columnar grains at the points of highest curvature along the melt pool reach a velocity at the limit of absolute stability [38,39]. Heat extraction will be highest at these points of highest curvature. This accelerates the growth of these columnar grains and facilitates the transformation interface acceleration and resultant partitionless solidification [59,60] of the alloy.

Based on the time-resolved images of Fig. 3, the tip radii of the eutectic columnar grains appear large and nearly planar, which is consistent with models [53] that indicate that the solid-liquid interface close to the limit of absolute stability should consist of morphologically flat-topped cells. A growth front that reaches this stability limit becomes morphologically unstable [38] and can undergo partitionless solidification (the partition coefficient approaches unity). Based on the models and qualitative interpretation of data used to construct Fig. 9, this stability limit should be accompanied by a sharp increase in the solidification front velocity of roughly an order of magnitude, as shown schematically in the figure. The light contrast, precipitate-free bands in the observed banded morphology (Fig. 7) can be attributed to the solidification front velocity reaching this absolute stability limit and ensuing partitionless solidification. Due to this morphological instability, the columnar grains that rapidly accelerated extend sufficiently far into the melt pool to prevent further growth along the thermal gradient, and the alloy can rapidly

solidify laterally along isotherms. By following the isotherms around the elliptical perimeter of the remaining melt pool these grains effectively prevent further growth of adjacent eutectic columnar grains in zone 3. This growth along isotherms is captured in the 25 μs image of Fig. 3(a), in which the solid-liquid interface of the precipitate-free band that is growing has advanced further laterally along an isotherm than in the direction toward the center of the melt pool along the major axis.

During this partitionless solidification, solute is no longer being rejected from the newly formed solid crystal into the liquid. The temperature of the kinetically modified eutectic liquid at the interface therefore increases, reducing the undercooling and causing the interface velocity to decrease gradually back below the absolute stability limit. This leads to solidification by the kinetically modified eutectic mode, generating the eutectic product again (dark bands). As a result the solidification front will advance with the chevron-like morphology observed in the time-resolved images and accelerate again to the absolute stability limit. This instability will be oscillatory overall, and both the velocity, as illustrated in Fig. 9, and undercooling (temperature) will fluctuate, with periodic variation in the growth direction [39]. Fig. 9 illustrates these oscillations and relates the velocity to the light and dark banding of the solidified banded structure, indicated at the bottom of the figure. The width of the eutectic (dark) bands has been observed to decrease as the banded structure solidifies (see Fig. 7), which is depicted schematically in Fig. 9. The width of the eutectic bands in the banded morphology solidification product has been determined to decrease by about a factor of five, e.g., from ~ 370 nm at the onset of the banded structure to ~ 70 nm when solidification is complete, as measured from Fig. 7. This indicates that during formation of the banded morphology grains the solidification front continued to accelerate, approaching velocities that would lead to complete partitionless

solidification (the width of the eutectic bands approaches zero as the velocity approaches this limit, though this was not observed in these *in-situ* TEM experiments). The number of oscillations included in Fig. 9 convey the number of bands observed in Fig. 7, with all 8 of these oscillations occurring in $\sim 10 \mu\text{s}$.

As indicated in Fig. 7, the central banded morphology consists of multiple columnar grains, both the type-2 grains that form the large banded structure and the type-3 “wraparound” grains. As shown in Fig. 7(c), these type-3 grains are banded, indicating that here the velocity of the absolute stability limit has also been reached. When type-3 columnar grains become unstable and partitionless solidification begins, further growth shifts to a lateral direction along an isotherm. However, the type-3 grains are constrained to grow in only one direction (away from the type-2 grain) along the available isotherm, as the type-2 grain, due to its growth along the axis of highest interface curvature and further protrusion into the melt pool, will prevent growth in both directions. This implies that the oscillatory instability that leads to banding is dependent on both heat extraction and local composition fluctuations [39] along the transformation front. Local composition fluctuations can create large, local undercoolings that produce high solidification front velocities in these regions. These composition fluctuations are further supported by the morphology of the banded structure, as seen in Fig. 7(c). While the transition from eutectic to partitionless solidification is abrupt and characterized by a smooth interface between the two different growth modes, the transition from partitionless growth back to eutectic growth along the thermal gradient produces a rough interface, indicating that the transition occurs at different times along the solid-liquid interface and is likely a result of local composition fluctuations along the front. Such an overall scenario as described here is suitable to

rationalize the morphology of the central banded morphology consisting of just a few large-scale grains and agrees with prior phenomenological [37] and phase-field [61,62] models.

5. Conclusions

Rapid solidification experiments conducted in the DTEM allowed *in-situ* observations of the evolution of the growth front morphology and quantification of solidification velocities with unprecedented spatial and temporal resolutions. Three microstructural zones were detected in the solidified microstructure. These microstructural zones were related to the changes in velocity of the solidification front and crystal growth-mode transitions during solidification. The solidification front was found to accelerate and three growth-mode transitions were discerned. The transitions in growth mode were accompanied by rapid acceleration and morphological instability at the solid-liquid interface. In particular, a morphological instability leading to formation of a banded structure was observed. The time-resolved TEM imaging experiments allowed, for the first time, direct observation of this structure during its growth, offering insight to the oscillatory mechanism of instability evolution and periodic variation in growth direction. The ability to capture these growth-mode changes *in situ* during rapid solidification still remains somewhat challenging due to the accelerations associated with instability development and evolution, even with the nanoscale spatiotemporal resolution afforded by the DTEM studies performed here. Finer temporal spacing between the images in a given series would allow observation with the required increased resolution in time to reveal additional mechanistic details of the crystal growth-mode transitions observed here during rapid solidification. For instance, the inferred acceleration-deceleration cycles associated with the growth-mode transitions during formation of the banded morphology could be quantitatively assessed. Further work will focus on performing such measurements using recent upgrades to the DTEM instrument that enable single-pump/multiple-image-acquisition experiments [46,47] of these rapid solidification processes.

Acknowledgments

This work was performed under the auspices of the U.S. Department of Energy by Lawrence Livermore National Laboratory and supported by the Office of Science, Office of Basic Energy Sciences, Division of Materials Science and Engineering of the U.S. Department of Energy under Contract No. DE-AC52-07NA27344. Work performed at the University of Pittsburgh received supported from the National Science Foundation, Division of Materials Research, Metals & Metallic Nanostructures program through Grant No. DMR 1105757. JTM would like to thank Dr. Joshua Sugar for access to and assistance with the JEOL 2010F TEM at Sandia National Laboratory in Livermore. Sandia is a multiprogram laboratory operated by Sandia Corporation, a Lockheed Martin Co., for the United States Department of Energy under Contract No. DE-AC04-94-AL85000.

References

- [1] Kline JE, Leonard JP. *Thin Solid Films* 2005;488.
- [2] Kline JE, Leonard JP. *Appl Phys Lett* 2005;86:201902.
- [3] Srivatsan TS, Sudarshan TS. *Rapid Solidification Technology—An Engineering Guide*, Technomic Publishing, Lancaster, PA, 1993.
- [4] Murray JL. *Int Met Rev* 1985;30:211.
- [5] Chen S-W, Huang C-C. *Acta Mater* 1996;44:1955.
- [6] Ólafsson P, Sandström R, Karlsson Å. *J Mater Sci* 1997;32:4383.
- [7] Poirier DR, McBride E. *Mater Sci Eng* 1997;A224:48.
- [8] Villars P. *ASM Alloy Phase Diagrams Center*. In: Okamoto H, Cenzual K, editors. *Materials Park, OH: ASM International*, 2006.
- [9] Scott MG, Leake JA. *Acta Metall* 1975;23:503.
- [10] Williams DB, Edington JW. *J Mater Sci* 1977;12:126.
- [11] Singh RK, Chattopadhyay K, Lele S, Anantharaman TR. *J Mater Sci* 1982;17:1617.
- [12] Sato T, Long TT, Tezuka H, Kamio A, Takahashi T. *J Jpn I Met* 1984;48:748.
- [13] Zimmermann M, Carrard M, Kurz W. *Acta Metall* 1989;37:3305.
- [14] Zimmermann M, Karma A, Carrard M. *Phys Rev B* 1990;42:833.
- [15] Zimmermann M, Carrard M, Gremaud M, Kurz W. *Mater Sci Eng A* 1991;134:1278.
- [16] Gill SC, Zimmermann M, Kurz W. *Acta Metall Mater* 1992;40:2895.
- [17] Gill SC, Kurz W. *Acta Metall Mater* 1993;41:3563.
- [18] Kurz W, Gilgien P. *Mater Sci Eng* 1994;A178:171.
- [19] Gill SC, Kurz W. *Acta Metall Mater* 1995;43:139.
- [20] Prasad A, Henein H, Maire E, Gandin C-A. *Metall Mater Trans A* 2006;37A:249.
- [21] Burden MH, Hunt JD. *J Cryst Growth* 1974;22:328.
- [22] Zhong R, Kulovits A, Wiezorek JMK, Leonard JP. *Appl Surf Sci* 2009;256:105.
- [23] Kulovits A, Zhong R, Wiezorek JMK, Leonard JP. *Thin Solid Films* 2009;517:3629.
- [24] Kulovits A, Wiezorek JMK, LaGrange T, Reed BW, Campbell GH. *Phil Mag Lett* 2011;91:287.
- [25] King WE, Campbell GH, Frank A, Reed B, Schmerge JF, Siwick BJ, et al. *J Appl Phys* 2005;97:111101.
- [26] LaGrange T, Armstrong MR, Boyden K, Brown CG, Campbell GH, Colvin JD, et al. *Appl Phys Lett* 2006;89:044105.
- [27] Kim JS, LaGrange T, Reed BW, Taheri M, Armstrong MR, King WE, et al. *Science* 2008;321:1472.
- [28] LaGrange T, Campbell GH, Reed BW, Taheri M, Pesavento JB, Kim JS, et al. *Ultramicroscopy* 2008;108:1441.
- [29] Reed BW, Armstrong MR, Browning ND, Campbell GH, Evans JE, LaGrange T, et al. *Microsc Microanal* 2009;15:272.
- [30] Browning ND, Campbell GH, Hawreliak JA, Kirk MA. *MRS Bull* 2010;35:1009.
- [31] Campbell GH, LaGrange T, Kim JS, Reed BW, Browning ND. *J Electron Microsc* 2010;59:S67.
- [32] Reed BW, LaGrange T, Shuttlesworth RM, Gibson DJ, Campbell GH, Browning ND. *Rev Sci Instrum* 2010;81:053706.
- [33] Kittl JA, Sanders PG, Aziz MJ, Brunco DP, Thompson MO. *Acta Mater* 2000;48:4797.
- [34] Boettinger WJ, Shechtman D, Schaefer RJ, Biancaniello FS. *Metall Trans A* 1984;15A:55.
- [35] Kurz W, Trivedi R. *Acta Metall Mater* 1990;38:1.
- [36] Gremaud M, Carrard M, Kurz W. *Acta Metall Mater* 1991;39:1431.
- [37] Carrard M, Gremaud M, Zimmermann M, Kurz W. *Acta Metall Mater* 1992;40:983.
- [38] Mullins WW, Sekerka RF. *J Appl Phys* 1964;35:444.
- [39] Coriell SR, Sekerka RF. *J Cryst Growth* 1983;61:499.
- [40] Pennycook SJ. *Ultramicroscopy* 1989;30:58.
- [41] Kulovits AK, Facco G, Wiezorek JMK. *Mater Charact* 2012;63:17.

- [42] Kurz W, Fisher DJ. Fundamentals of Solidification, Trans Tech SA, Switzerland, 1984.
- [43] Vincent R, Midgley P. Ultramicroscopy 1994;53:271.
- [44] Rauch EF, Veron M, Portillo J, Bultreys D, Maniette Y, Nicolopoulos S. Microsc Anal 2008;22:S5.
- [45] Portillo J, Rauch EF, Nicolopoulos S, Gemmi M, Bultreys D. Mater Sci Forum 2010;644:1.
- [46] LaGrange T, Reed BW, Santala MK, McKeown JT, Kulovits A, Wiezorek JMK, et al. Micron 2012;43:1108.
- [47] Santala MK, Reed BW, Raoux S, Topuria T, LaGrange T, Campbell GH. Appl Phys Lett 2013;102:174105.
- [48] Prokhorov AM, Konov VI, Ursu I, Mihailsecu IN. Laser Heating of Metals, Adam Hilger, IOP Publishing Ltd., Philadelphia, 1990.
- [49] Boyden SB, Zhang Y. J Thermophys Heat Tr 2006;20:9.
- [50] Siwick BJ, Dwyer JR, Jordan RE, Miller RJD. Science 2003;302.
- [51] Rocha OL, Siqueira CA, Garcia A. Metall Mater Trans A 2003;34:995.
- [52] Zink BL, Hellman F. Solid State Commun 2004;129:199.
- [53] Kurz W, Fisher DJ. Acta Metall 1981;29:11.
- [54] Burden MH, Hunt JD. J Cryst Growth 1974;22:99.
- [55] Burden MH, Hunt JD. J Cryst Growth 1974;22:109.
- [56] Boettinger WJ. Growth kinetic limitations during rapid solidification. In: Kear BH, Giessen BC, Cohen M, editors. Rapidly Solidified Amorphous and Crystalline Alloys. New York: Elsevier Science Publishing Co., Inc., 1982. p.15.
- [57] Dean H, Gruzleski JE. J Cryst Growth 1973;20:256.
- [58] Boettinger WJ, Perepezko JH. Fundamentals of solidification at high rates. In: Liebermann HH, editor. Rapidly Solidified Alloys: Processes, Structures, Properties, Applications. New York: Marcel Dekker, Inc., 1993.
- [59] Aziz MJ, Kaplan T. Acta Metall 1988;36:2335.
- [60] Baker JC, Cahn JW. Acta Metall 1969;17:575.
- [61] Conti M. Phys Rev E 1998;58:6101.
- [62] Conti M. Phys Rev E 1998;58:6166.
- [63] Yota J, Hander J, Saleh AA. J Vac Sci Technol 2000;18.

Figures

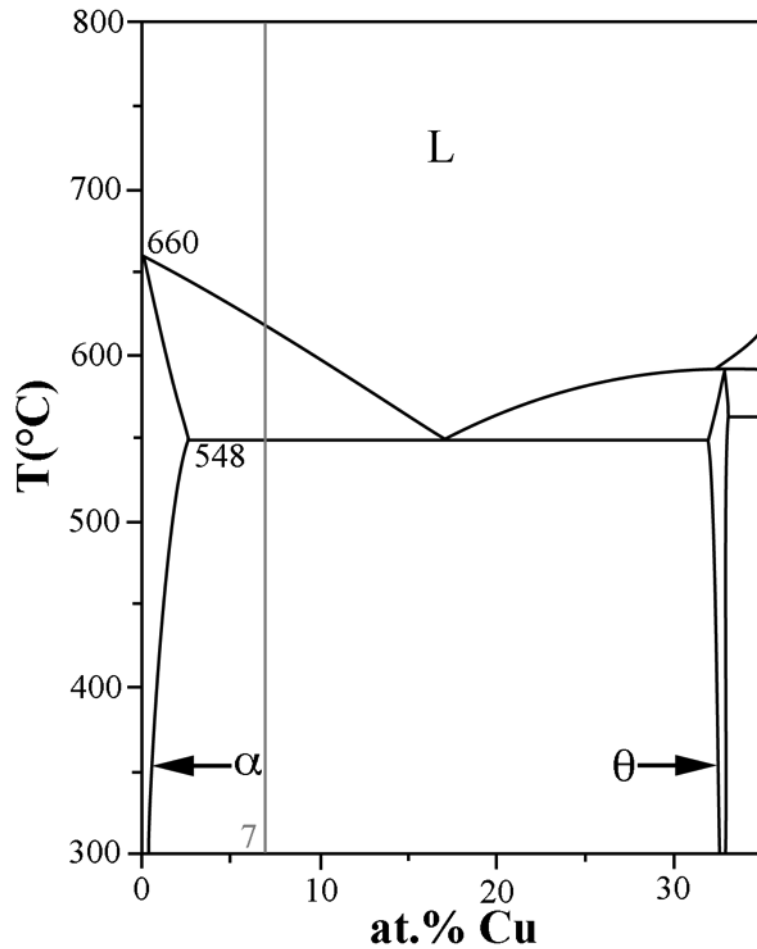


Fig. 1. Al-rich portion of the Al-Cu equilibrium phase diagram, showing the eutectic with terminal phases of α -Al and θ -Al₂Cu. The eutectic temperature and composition are 548°C and ~17at%, respectively. The hypoeutectic alloys investigated in this study had composition Al-7at%Cu, as indicated on the phase diagram. Reproduced after reference [8].

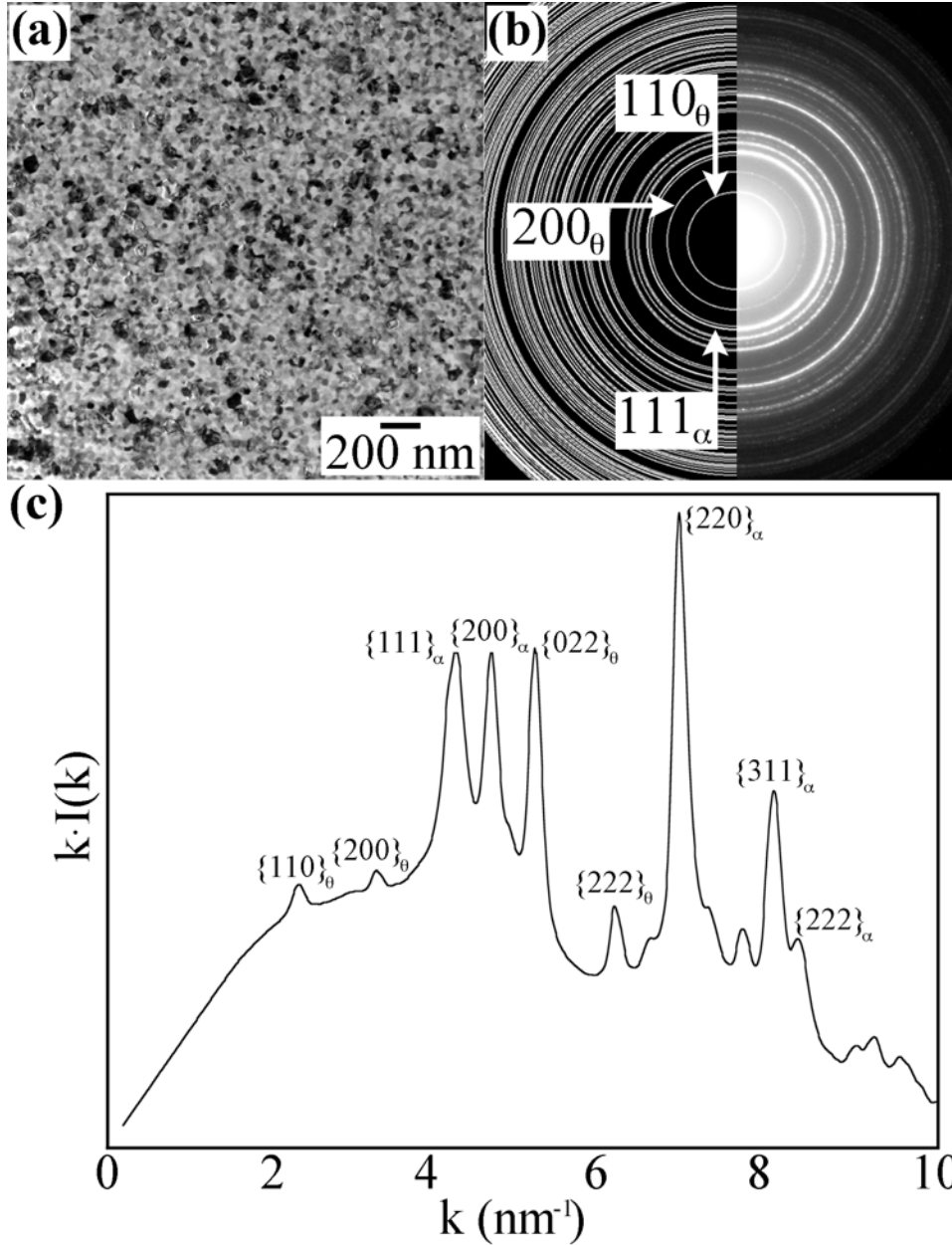


Fig. 2. (a) BF TEM image of the initial, nanocrystalline Al-7at.%Cu thin film prior to solidification experiments. (b) Experimental selected-area diffraction pattern (right) from the initial, as-deposited thin film with a simulated diffraction pattern (left), showing that the film consisted of both the α -Al and θ -Al₂Cu phases. (c) Rotationally integrated profile of the experimental diffraction pattern in (b). For reference, the two innermost diffraction rings correspond to the $\{110\}$ (2.33 nm⁻¹) and $\{200\}$ (3.30 nm⁻¹) planes of the θ phase. The third diffraction ring corresponds to an overlap of the $\{002\}$ (4.10 nm⁻¹) and $\{121\}$ (4.22 nm⁻¹) planes of the θ phase with the $\{111\}$ (4.27 nm⁻¹) planes of the α -Al phase.

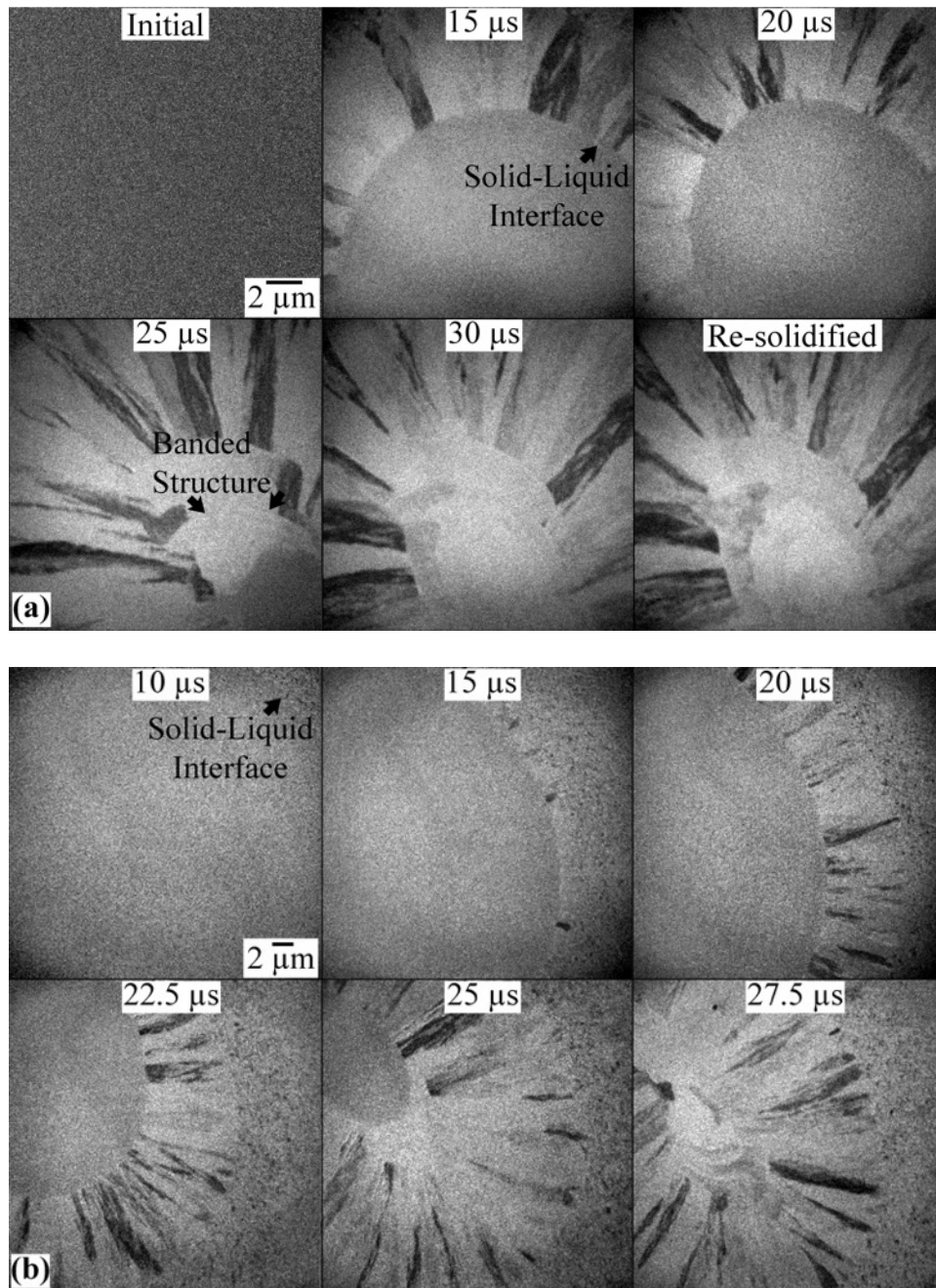


Fig. 3. BF 15-ns-exposure TEM images recorded before and at multiple time delays after laser melting of an Al-7at.%Cu alloy. Scale bars in upper left apply to all images in (a) and (b), respectively. Images in (a) and (b) were recorded at different magnifications to capture various features of the microstructure during solidification.

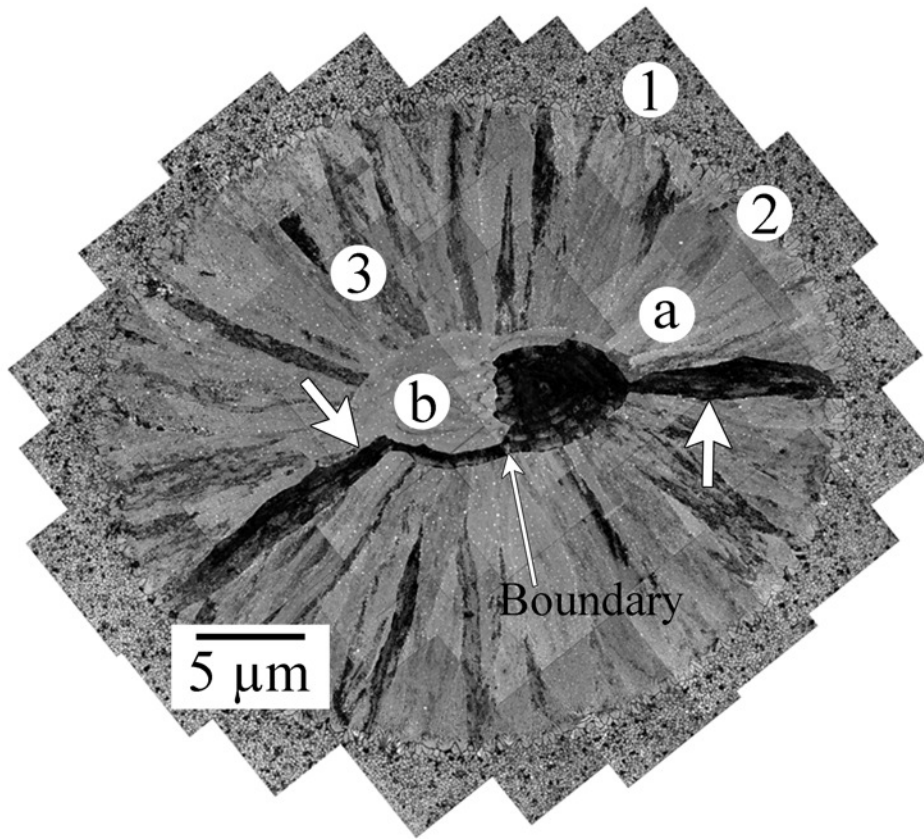


Fig. 4. Montage of conventional BF TEM images showing three distinct morphological zones in the re-solidified alloy film: (1) heat-affected zone containing a hypoeutectic structure, (2) a transition zone, and (3) a growth zone that contains (a) a columnar region that produces (b) large central grains with a banded structure. Large arrows indicate two separate columnar grains that are separated by a grain boundary, as indicated. Both arrowed columnar grains are in a $[011]$ zone axis.

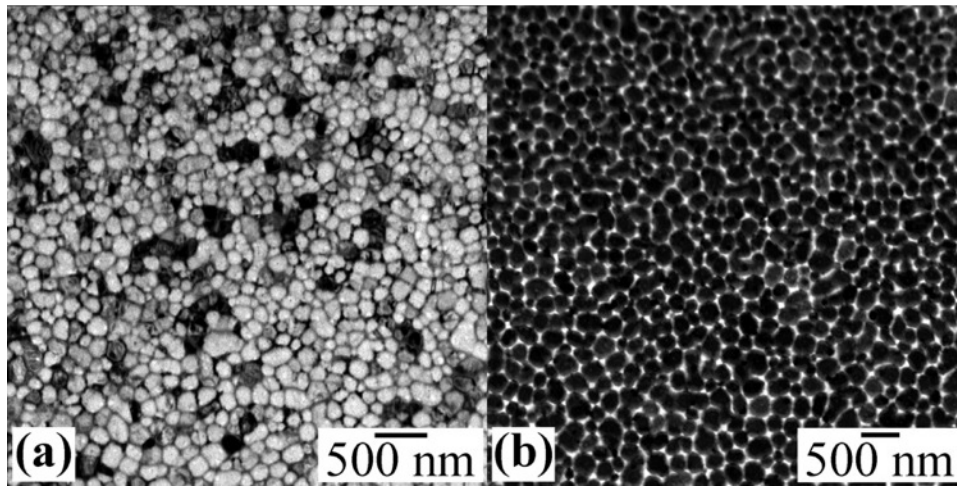


Fig. 5. *Zone I Microstructure*: (a) BF TEM and (b) ADF STEM images of the hypoeutectic structure in the heat-affected zone.

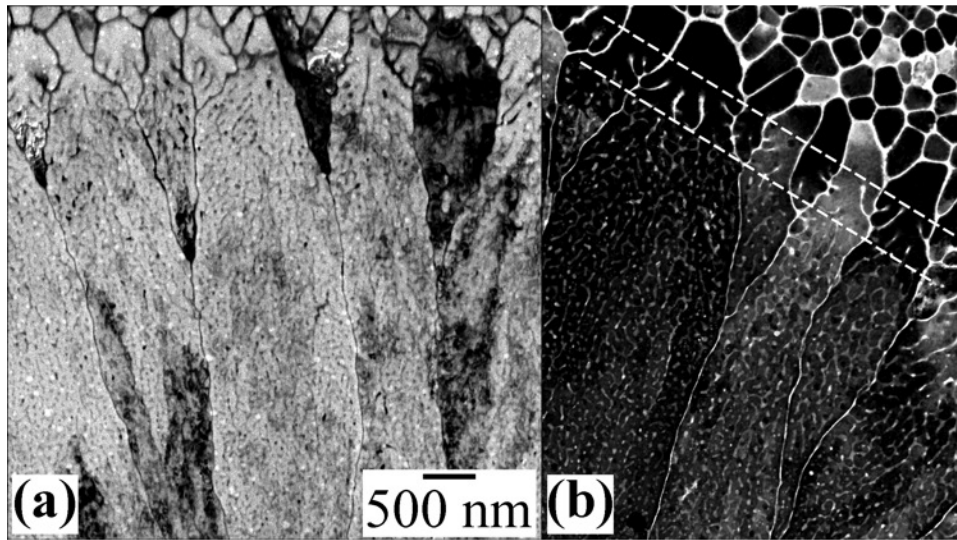


Fig. 6. *Zone 2 Microstructure*: (a) BF TEM and (b) ADF STEM images of the transition zone. Scale bar applies to (a) and (b). The upper dashed line indicates a transition to cellular/dendritic growth. The lower dashed line indicates a transition from cellular to columnar growth, with a concurrent growth-mode change from a hypoeutectic growth mode with pro-eutectic α -Al to eutectic solidification.

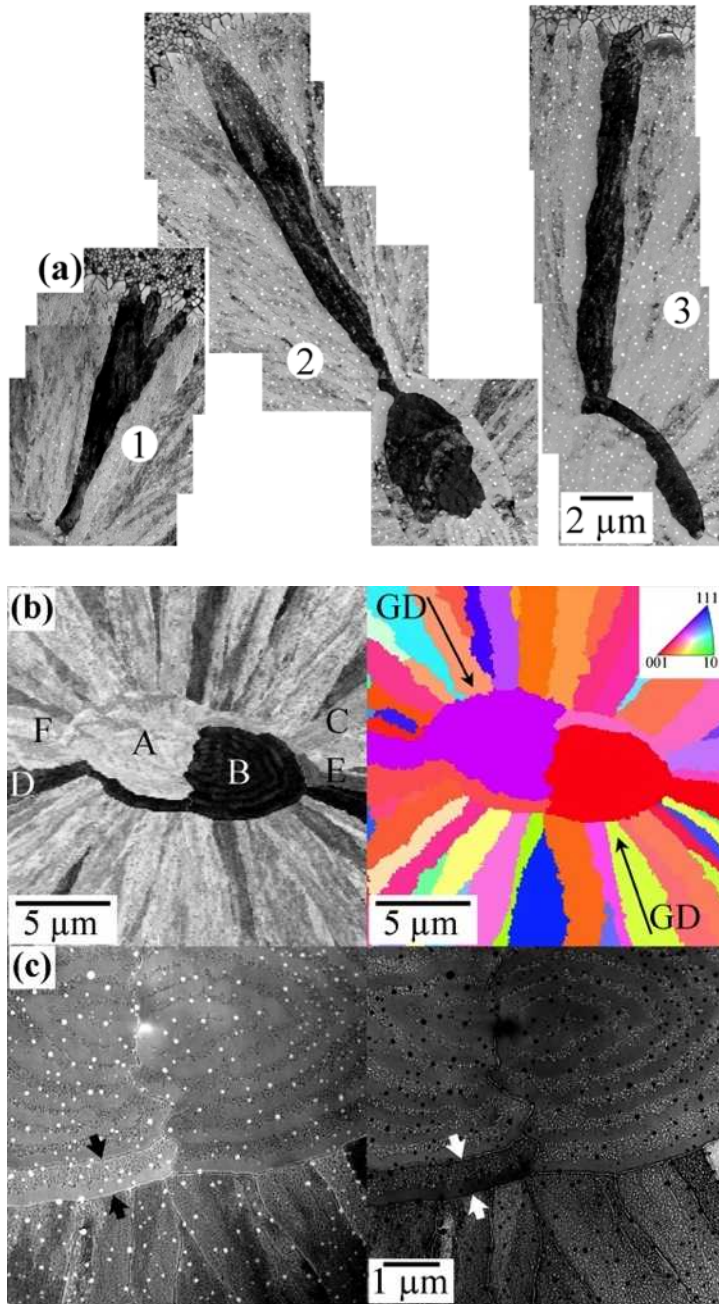


Fig. 7. *Zone 3 Microstructure*: (a) BF TEM montage images of columnar grains tilted into zone-axis orientations. The numerical labels indicate the three types of columnar morphologies. (b) Virtual BF image and corresponding orientation map of the growth directions (GD). The standard triangle orientation legend corresponds to the GD in the plane of the film (parallel to the film-substrate interface). The grains labeled A–F constitute the central banded morphology. (c) BF and corresponding HAADF STEM images showing the central banded structure. The black/white arrows indicate a “wraparound” type-3 columnar grain, showing that these grains are also banded. The images in Fig. 7 also show the presence of pinholes in the film. These holes are

prevalent throughout the re-solidified alloy and likely due to the hydrogen outgassing of the amorphous silicon nitride membrane substrates [63].

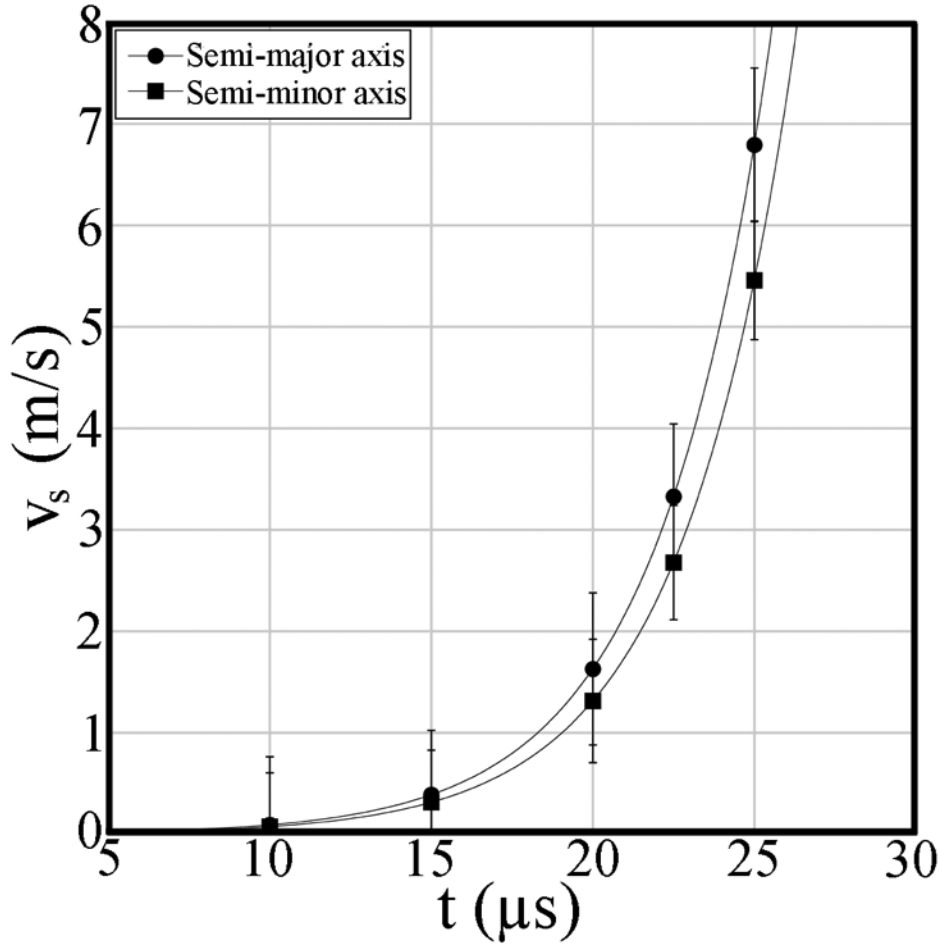


Fig. 8. Plot of the velocity of the solidification front with time along the semi-major and semi-minor axes of the elliptical melt pool, as indicated, for the hypoeutectic Al-7at%Cu alloy, showing that the solid-liquid interface is accelerating. Error bars were calculated by considering two additive effects: motion blur and the shot-to-shot fluctuation in the energy of the laser used to melt the alloy films. The error due to motion blur was calculated by multiplying the velocity at time t (in nm/ns) by the temporal resolution of 15 ns (the duration of the electron pulse used to capture the time-resolved images). The fluctuation in the laser energy, ΔE , has been characterized to vary by $\sim \pm 2.5\%$. This will produce variations in the semi-major and semi-minor axes of the initial melt pool, a_0 and b_0 , between experiments with different delay times. As an approximation, consider the energy required to create an elliptical melt pool:

$\Delta Q = n(C_p \Delta T + L_f)$, where n is the number of moles, C_p is the molar heat capacity, ΔT is the temperature change from room temperature to the melting temperature, and L_f is the molar latent heat of fusion. The number of moles will be proportional to the volume of the initial elliptical melt pool, given by $V = \frac{1}{2} \pi a_0 b_0 h$, where h is the film thickness. Thus, the fluctuations in the semi-major and semi-minor axes of the initial melt pool, a_0 and b_0 , will vary by $\sim \pm 1.25\%$.

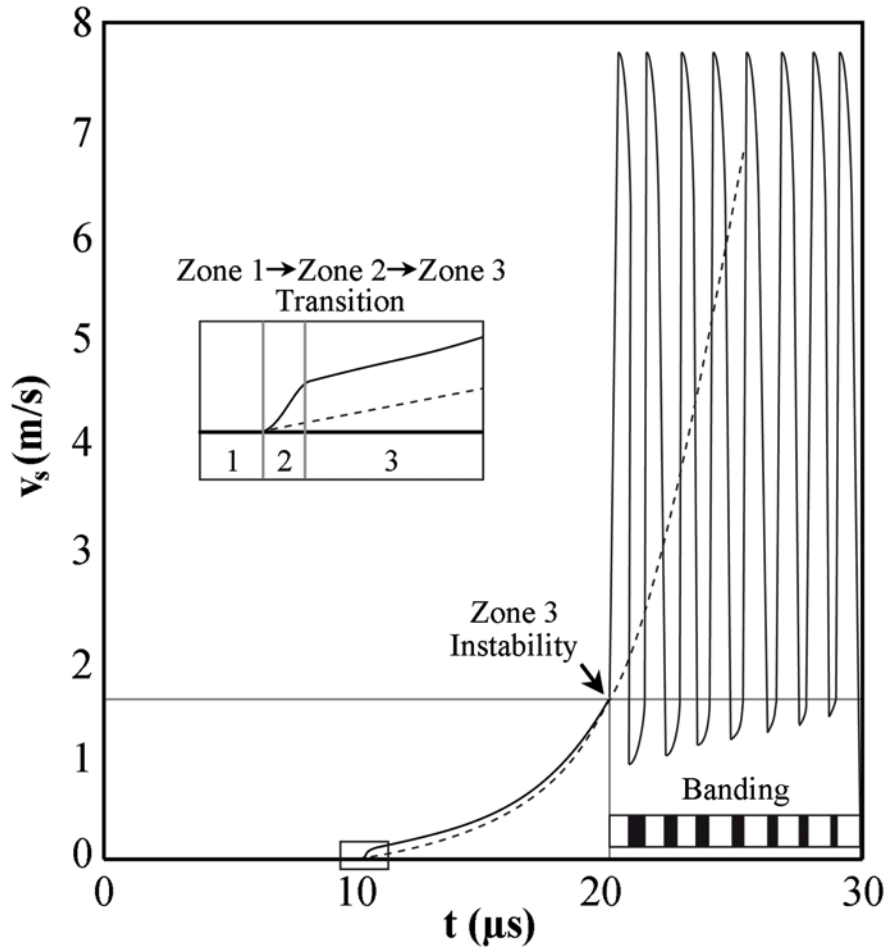


Fig. 9. Experimentally measured (dashed curve) and qualitatively assessed (solid curve) plot of the time-varying evolution of the solidification front velocity. The inset shows the rapid transition from zone 1 to zone 2 to zone 3 growth. The instability that leads to the banded structure in zone 3 is indicated by the arrow and the sudden increase in velocity at $\sim 20 \mu s$, and the banding that occurs in the microstructure during solidification is indicated by the dark and light bands below the velocity plot. The bands shown over the final $10 \mu s$ of the figure relate to the number, width, and spacing of the bands observed in Fig. 7.